Structure-based modeling of SARS-CoV-2 peptide/HLA-A02 antigens

Santrupti Nerli[1] and Nikolaos G. Sgourakis[2]
Email: nsgourak@ucsc.edu

[1]Department of Biomolecular Engineering, University of California Santa Cruz, Santa Cruz, CA 95064, USA.
[2]Department of Chemistry and Biochemistry, University of California Santa Cruz, Santa Cruz, CA 95064, USA.

ABSTRACT
As a first step toward the development of diagnostic and therapeutic tools to fight the Coronavirus disease (COVID-19), it is important to characterize CD8+ T cell epitopes in the SARS-CoV-2 peptidome that can trigger adaptive immune responses. Here, we use RosettaMHC, a comparative modeling approach which leverages existing high-resolution X-ray structures from peptide/MHC complexes available in the Protein Data Bank, to derive physically realistic 3D models for high-affinity SARS-CoV-2 epitopes. We outline an application of our method to model 439 9mer and 279 10mer predicted epitopes displayed by the common allele HLA-A*02:01, and we make our models publicly available through an online database (https://rosettamhc.chemistry.ucsc.edu). As more detailed studies on antigen-specific T cell recognition become available, RosettaMHC models of antigens from different strains and HLA alleles can be used as a basis to understand the link between peptide/HLA complex structure and surface chemistry with immunogenicity, in the context of SARS-CoV-2 infection.

An ongoing pandemic caused by the novel SARS coronavirus (SARS-CoV-2) has become the focus of extensive efforts to develop vaccines and antiviral therapies (1). Immune modulatory interferons, which promote a widespread antiviral reaction in infected cells, and inhibition of pro-inflammatory cytokine function through anti-IL-6/IL-6R antibodies, have been proposed as possible COVID-19 therapies (2, 3). However, stimulating a targeted T cell response against specific viral antigens is hampered by a lack of detailed knowledge of the immunodominant epitopes displayed by common Human Leukocyte Antigen (HLA) alleles across individuals (public epitopes). The molecules of the class I major histocompatibility complex (MHC-I, or HLA in humans) display on the cell surface a diverse pool of 8 to 15 amino acid peptides derived from the endogenous processing of proteins expressed inside the cell (4). This MHC-I restriction of peptide antigens provides jawed vertebrates with an essential mechanism for adaptive immunity: surveillance of the displayed peptide/MHC-I (pMHC-I) molecules by CD8+ cytotoxic T-lymphocytes allows detection of aberrant protein expression patterns, which signify viral infection and can trigger an adaptive immune response (5). A recent study has shown important changes in T cell compartments during the acute phase of SARS-CoV-2 infection (6), suggesting that the ability to quantify antigen-specific T cells would provide new avenues for understanding the

expansion and contraction of the TCR repertoire in different disease cohorts and clinical settings. Given the reduction in breadth and functionality of the naïve T cell repertoire during aging (7), identifying a minimal set of viral antigens that can elicit a protective response will enable the design of diagnostic tools to monitor critical gaps in the T cell repertoire of high-risk cohorts, which can be addressed using peptide or epitope string DNA vaccines (8).

Human MHC-I molecules are extremely polymorphic, with thousands of known alleles in the classical HLA-A, -B and -C loci. Specific amino acid polymorphisms along the peptide-binding groove (termed A-F pockets) define a repertoire of 10^4-10^6 peptide antigens that can be recognized by each HLA allotype (9, 10). Several machine-learning methods have been developed to predict the likelihood that a target peptide will bind to a given allele (reviewed in (11)). Generally these methods make use of available data sets in the Immune Epitope Database (12) to train artificial neural networks that predict peptide processing, binding and display, and their performance varies depending on peptide length and HLA allele representation in the database. Structure-based approaches have also been proposed to model the bound peptide conformation *de novo* (reviewed in (13)). These approaches utilize various algorithms to optimize the backbone and side chain degrees of freedom of the peptide/MHC structure according to an all-atom scoring function, derived from physical principles (14–16), that can be further enhanced using modified scoring terms (17) or mean field theory (18). While these methods do not rely on large training data sets, their performance is affected by bottlenecks in sampling of different backbone conformations, and any possible structural adaptations of the HLA peptide-binding groove.

Predicting the bound peptide conformation whose N- and C- termini are anchored within a fixed-length groove is a tractable modeling problem that can be addressed using standard comparative modeling approaches (19). In previous work focusing on the HLA-B*15:01 and HLA-A*01:01 alleles in the context of neuroblastoma neoantigens, we have found that a combined backbone and side chain optimization approach can yield accurate pMHC-I models for a pool of target peptides, provided that a reliable template of the same allele and peptide length can be identified in the database (20). In this approach (RosettaMHC), a local optimization of the backbone degrees of freedom is sufficient to capture minor (within 0.5 Å heavy atom RMSD) changes of the target peptide backbone relative to the conformation of the peptide in the template, used as a starting point. For HLA-A*02:01, the most common HLA allele among disease-relevant population cohorts (21), there is a large number of high-resolution X-ray structures available in the PDB (22), suggesting that a similar principle can be applied to produce models of candidate epitopes directly from the proteome of a pathogen of interest. Here, we apply RosettaMHC to all HLA-A*02:01 epitopes predicted directly from the ~30 kbp SARS-CoV-2 genome, and make our models publicly available through an online database. The computed binding energies of our models can be used as an additional validation layer to select high-affinity epitopes from large peptide sets. As detailed epitope mapping data from high-throughput tetramer staining (23–25) and T cell functional screens (26) become available, the models presented here can provide a toehold for understanding links between pMHC-I antigen structure and immunogenicity, with actionable value for the development of peptide vaccines to combat the disease.

Materials and Methods

Identification of SARS-CoV-2 peptide epitopes

The SARS-CoV-2 protein sequences (https://www.ncbi.nlm.nih.gov/nuccore/NC_045512.2) were obtained from NCBI and used to generate all possible peptides of lengths 9 and 10 (9,621 9mer and 9,611 10mer peptides). We used NetMHCpan-4.0 (27) to derive binding scores to HLA-A*02:01, and retained only peptides classified as strong or weak binders (selected using the default percentile rank cut-off values). The binding classification was performed using eluted ligand likelihood predictions. While in this study we use NetMHCpan-4.0 predictions as inputs to select candidate epitopes for structure modeling, our workflow is fully compatible with any alternative epitope prediction method.

Selection of PDB templates

To model SARS-CoV-2 / HLA-A*02:01 antigens, we identified 3D structures from the PDB that can be used as templates for comparative modeling. First, we selected all HLA-A02 X-ray structures that are below 3.5 Å resolution and retained only those that have 100% identity to the HLA-A*02:01 heavy chain sequence (residues 1-180). We found 241 template structures bound to epitopes of lengths from 8 to 15 residues (of which 170 are 9mers and 61 are 10mers). For each SARS-CoV-2 target peptide, we selected a set of candidate templates of the same length by matching the target peptide anchor positions (P2 and P9/P10) to each peptide in the template structures. Then, we used the BLOSUM62 (28) substitution matrix to score all remaining positions in the pairwise alignment of the target/template sequences, and the PDB template with the top alignment score was selected for modeling. For target peptides where we found no templates which match both peptide anchors, we scored all positions in the pairwise alignment and selected the top scoring template for modeling.

RosettaMHC modeling framework and database

RosettaMHC (manuscript in preparation) is a comparative modeling protocol developed using PyRosetta (29) to model pMHC-I complexes. The program accepts as input a list of peptide sequences, an HLA allele definition and a template PDB file (selected as described in the previous step). To minimize "noise" in the simulation from parts of the MHC-I fold that do not contribute to peptide binding, only the α_1 and α_2 domains are considered in all steps. For each peptide, a full alignment between the target and template peptide/MHC sequences is performed using clustal omega (30). The alignment is used as input to Rosetta's threading protocol (*partial_thread.<ext>*). From the threaded model, all residues in the MHC-I groove that are within a heavy-atom distance of 3.5 Å from the peptide are subjected to 10 independent all-atom refinement simulations using the FastRelax method (31) and a custom movemap file. Binding energies are extracted from the refined structures using interface analyzer protocol (*InterfaceAnalyzer.<ext>*). The top three models are selected based on the binding energies, and used to compute an average energy for each peptide in the input list. RosettaMHC models of SARS-CoV-2/HLA-A*02:01 epitopes are

made available through an online database (see data availability). The website that hosts our database was constructed using the Django web framework.

Results and Discussion

Template identification for structure modeling using RosettaMHC

Our full workflow for template identification and structure modeling is outlined in Figure 1a, with a flowchart shown in Figure 1b. To identify all possible regular peptide binders to HLA-A*02:01 that are expressed by SARS-CoV-2, we used a recently annotated version of all open reading frames (ORFs) in the viral genome from NCBI (32), made available through the UCSC genome browser (33). We used 9- and 10- residue sliding windows to scan all protein sequences, since these are the optimum peptide lengths for binding to the HLA-A*02:01 groove (34). While spliced peptide epitopes (35) are not considered in the current study, this functionality can be added to our method at a later stage. Using NetMHCpan-4.0 (27), we identified all 439 9mer and 279 10mer epitopes that are predicted to yield positive (classified as both weak and strong) binders. To further validate this set and derive plausible 3D models of the peptide/HLA-A*02:01 complexes, we used a structure-guided approach, RosettaMHC, which aims to derive a physically realistic fitness score for each peptide in the HLA-A*02:01 binding groove using an annotated database of high-resolution structures and Rosetta's all-atom energy function (36). RosettaMHC leverages a database of 241 HLA-A*02:01 X-ray structures encompassing a range of bound peptides, to find the closest match to each target epitope predicted from the SARS-CoV-2 proteome. To identify the best template for structure modeling, we use sequence matching criteria which first consider the peptide anchors (positions P2 and P9/P10 for 9mer/10mer epitopes), followed by a sequence similarity metric calculated from the full alignment between the template and target peptide sequences. The template assignment statistics for the four different classes of SARS-CoV-2 epitopes in our set are shown in Figure 2a. We find that we can cover the entire set of 718 predicted binders using a subset of 114 HLA-A*02:01 templates in our annotated database of PDB-derived structures (Figure 2b). Each target peptide sequence is then threaded onto the backbone of its best identified template, followed by all-atom refinement of the side chain and backbone degrees of freedom using Rosetta's Ref2015 energy function (36), and binding energy calculation.

RosettaMHC models recapitulate features of high-resolution X-ray structures

The sequence logos derived from 9mer and 10mer peptides with good structural complementarity to the HLA-A*02:01 groove according to Rosetta's binding energy (see below) adhere to the canonical motif, with a preference for hydrophobic, methyl-bearing side chains at the peptide anchor residues P2 and P9 (Figure 3a). The anchor residue preferences are recapitulated in representative 9mer and 10mer models of the two top binders in our set as ranked by Rosetta's energy (Figure 3c and 3d), corresponding to epitopes TMADLVYAL and FLFVAAIFYL derived from the RNA polymerase and nsp3 proteins, respectively, which are both encoded by *orf1ab* in

the viral genome (NCBI Reference YP_009724389.1). In accordance with features seen in high-resolution structures of HLA-A*02:01-restricted epitopes, the peptides adopt an extended, bulged backbone conformation. The free N-terminus of both peptides is stabilized by a network of polar contacts with Tyr 7, Tyr 159, Tyr 171 and Glu 63 in the A- and B- pockets of the HLA-A*02:01 groove. The Met (9mer) or Leu (10mer) side chain of P2 is buried in a B-pocket hydrophobic cleft formed by Met 45 and Val 67. Equivalently, the C-terminus is coordinated through polar contacts with Asp 77 and Lys 145 from opposite sides of the groove, with the Leu P9/P10 anchor nestled in the F-pocket defined by the side chains of Leu 81, Tyr 116, Tyr 123 and Trp 147. Residues P3-P8 form a series of backbone and side chain contacts with pockets C, D and E, while most backbone amide and carbonyl groups form hydrogen bonds with the side chains of residues lining the MHC-I groove. These high-resolution structural features are consistent across low-energy models of unrelated target peptides in our input set, suggesting that, when provided with a large set of input templates, a combined threading and side chain optimization protocol can derive physically realistic models.

Selection of high-affinity peptide epitopes using a structure-based score

To evaluate the accuracy of our models and fitness of each peptide within the HLA-A*02:01 binding groove, we computed Rosetta all-atom binding energies across all complexes modeled for different peptide sets. High binding energies can be used as an additional metric to filter low-affinity peptides in the NetMHCpan-4.0 predictions, with the caveat that high energies can be also due to incomplete optimization of the Rosetta energy function as a result of significant deviations between the target and template backbone conformations, not captured by our protocol. We performed 10 independent calculations for each peptide, and the 3 lower-energy models were selected as the final ensemble and used to compute an average binding energy. The results for all 9mer peptides are summarized in Figures 3e, f, while additional results for 10mers are provided through our web-interface and outlined in Supplemental Table 1. As a positive reference, we used the binding energies of the idealized and relaxed PDB templates, which are at a local minimum of the Rosetta scoring function. As a reference set for sub-optimal binders, we modeled decoy structures of poly alanine (polyA) peptide sequences (predicted by NetMHCpan-4.0 to be a top 9th percentile binder for HLA-A*02:01), threaded onto the same PDB templates.

We observe a significant, negative (-26 kcal/mol) energy gap between the average binding energies for PDB templates and poly alanine models. The binding energies for all modeled 9mers from the SARS-CoV-2 genome fall between the average energies of the optimal PDB templates and sub-optimal polyA binders, and show a bimodal distribution with significant overlap with the refined PDB template energies (Figure 1e). Comparison of the distributions between epitopes that are classified as strong versus weak binders by NetMHCpan-4.0 shows a moderate bias towards lower binding energies for the strong binders and a larger spread in energies for weak binders, likely due to suboptimal residues at the P2 and P9 anchor positions (Figure 3f). As an intendent positive set, we also modeled 28 9mer peptides that are homologous to peptides in the SARS viral genome and

200 have been previously reported to bind HLA-A*02:01 in the IEDB and ViPR (12, 37, 38) databases
201 (Supplemental Table 2). Inspection of Rosetta binding energies derived from models in this set
202 shows a similar distribution to the epitopes classified by NetMHCpan-4.0 as strong binders, with
203 the energies of 19/28 peptides falling well within the distribution of the refined PDB templates
204 (red dots in Figure 3e).
205
206 Based on these observations, we further classified all epitopes in the original set provided by
207 NetMHCpan-4.0 as strong or weak binders according to the Rosetta binding energy. Peptides with
208 binding energies that fall well within the PDB template distribution (green curve and red dots in
209 Figure 3e) are classified as strong binders. We obtained 154 9mer and 72 10mer strong binders
210 which show optimal complementarity within the HLA-A*02:01 peptide-binding groove according
211 to our modeling simulations. These results suggest that the high-resolution features seen in our
212 models (Figure 3c, d) yield optimal binding energies for a significant fraction of the epitopes
213 predicted by NetMHCpan-4.0 (45/33% of strong binders and 30/25% of weak binders for
214 9mers/10mers, respectively), which are comparable to locally refined PDB structures. The average
215 binding energies for all peptides are provided in our web-interface and in Supplemental Table 1.
216
217 *Surface features of peptide/HLA-A*02:01 models for T cell recognition*
218 Visualization of our models through an interactive online interface provides direct information on
219 SARS-CoV-2 peptide residues that are bulging out of the MHC-I groove, and are therefore
220 accessible to interactions with complementarity-determining regions (CDRs) of T cell receptors
221 (TCRs). Given that αβ TCRs generally employ a diagonal binding mode to engage pMHC-I
222 antigens where the CDR3α and CDR3β TCR loops form direct contacts with key peptide residues
223 (39, 40), knowledge of the surface features for different epitopes adds an extra layer of information
224 to interpret sequence variability between different viral strains. For other important antigens with
225 known structures in the PDB, such features can be derived from an annotated database connecting
226 pMHC-I/TCR co-crystal structures with biophysical binding data (41), and were recently
227 employed in an artificial neural network approach to predict the immunogenicity of different HLA-
228 A*02:01 bound peptides in the context of tumor neoantigen display (42). A separate study has
229 shown that the electrostatic compatibility between self vs foreign HLA surfaces can be used to
230 determine antibody alloimmune responses (43). Given that antibodies and TCRs use a common
231 fold and similar principles to engage pMHC-I molecules (40), it is likely that surface electrostatic
232 features play an important role in recognition of peptide/HLA surfaces by their cognate TCRs in
233 the context of SARS-CoV-2 infection.
234 Electrostatic surface potentials calculated using a numerical solution to the Poisson-Boltzmann
235 Equation (44) for our modeled peptide/HLA-A*02:01 complexes allow us to compare important
236 features for TCR recognition between different high-affinity epitopes (Figure 4). We observe a
237 moderate electropositive character of the HLA-A*02:01 α_1 helix, and a moderate negative
238 potential on the α_2 helix, which is consistent between complexes with different bound peptides.
239 However, due to substantial sequence variability in surface-exposed residues at the P2-P8

positions, we observe a range of electrostatic features ranging from negative (epitope TMADLVYAL), to neutral (NLIDSYFVV) or positively charged (KLWAQCVQL). Further classification and ranking of the top binders in our set on the basis of their molecular surface features would enable the selection of the most diverse panel of peptides for high-throughput pMHC tetramer library generation (23-25). Tetramer screening of T cells from COVID-19 patients, recovered individuals and healthy donors can be used to identify critical gaps in the T cell repertoire of high-risk groups, and to design epitope DNA strings for vaccine development.

Acknowledgements

The authors are grateful to Alison Lindberg and ITS/ADC staff at UCSC for assistance in setting up the web server for the database, and Hiram Clawson (UCSC Genome Browser) for providing the SARS-CoV-2 protein sequence data. We thank Andrew McShan, Hailey Wallace (UCSC) for assistance in the development of the RosettaMHC protocol, and David Haussler (UCSC), Michael Betts (University of Pennsylvania) and David Margulies (NIH) for helpful discussions. This work was supported through Grants from NIAID (5R01AI143997) and NIGMS (5R35GM125034).

Code and Data availability

An online web-interface for visualization and download of all models is available at: https://rosettamhc.chemistry.ucsc.edu. The RosettaMHC source code is available at https://github.com/snerligit/mhc-pep-threader. Rosetta binding energies for all 718 HLA-A*02:01-restricted peptides in our set are provided in Supplemental Table 1.

Disclosures

The authors have no financial conflicts of interest.

References

1. Liu, C., Q. Zhou, Y. Li, L. V. Garner, S. P. Watkins, L. J. Carter, J. Smoot, A. C. Gregg, A. D. Daniels, S. Jervey, and D. Albaiu. 2020. Research and Development on Therapeutic Agents and Vaccines for COVID-19 and Related Human Coronavirus Diseases. *ACS Cent. Sci.* .

2. Kumaki, Y., J. Ennis, R. Rahbar, J. D. Turner, M. K. Wandersee, A. J. Smith, K. W. Bailey, Z. G. Vest, J. R. Madsen, J. K.-K. Li, and D. L. Barnard. 2011. Single-dose intranasal administration with mDEF201 (adenovirus vectored mouse interferon-alpha) confers protection from mortality in a lethal SARS-CoV BALB/c mouse model. *Antiviral Res.* 89: 75–82.

3. Kishimoto, T. 2006. Interleukin-6: discovery of a pleiotropic cytokine. *Arthritis Res. Ther.* 8: S2.

4. Rock, K. L., E. Reits, and J. Neefjes. 2016. Present Yourself! By MHC Class I and MHC Class II Molecules. *Trends Immunol.* 37: 724–737.

5. Kaufman, J. 2018. Unfinished Business: Evolution of the MHC and the Adaptive Immune System of Jawed Vertebrates. *Annu. Rev. Immunol.* 36: 383–409.

6. Thevarajan, I., T. H. O. Nguyen, M. Koutsakos, J. Druce, L. Caly, C. E. van de Sandt, X. Jia, S. Nicholson, M. Catton, B. Cowie, S. Y. C. Tong, S. R. Lewin, and K. Kedzierska. 2020.

Breadth of concomitant immune responses prior to patient recovery: a case report of non-severe COVID-19. *Nat. Med.* 1–3.
7. Goronzy, J. J., F. Fang, M. M. Cavanagh, Q. Qi, and C. M. Weyand. 2015. Naïve T cell maintenance and function in human aging. *J. Immunol. Baltim. Md 1950* 194: 4073–4080.
8. Oyarzun, P., and B. Kobe. 2015. Computer-aided design of T-cell epitope-based vaccines: addressing population coverage. *Int. J. Immunogenet.* 42: 313–321.
9. Birnbaum, M. E., J. L. Mendoza, D. K. Sethi, S. Dong, J. Glanville, J. Dobbins, E. Ozkan, M. M. Davis, K. W. Wucherpfennig, and K. C. Garcia. 2014. Deconstructing the peptide-MHC specificity of T cell recognition. *Cell* 157: 1073–1087.
10. Wooldridge, L., J. Ekeruche-Makinde, H. A. van den Berg, A. Skowera, J. J. Miles, M. P. Tan, G. Dolton, M. Clement, S. Llewellyn-Lacey, D. A. Price, M. Peakman, and A. K. Sewell. 2012. A single autoimmune T cell receptor recognizes more than a million different peptides. *J. Biol. Chem.* 287: 1168–1177.
11. Peters, B., M. Nielsen, and A. Sette. 2020. T Cell Epitope Predictions. *Annu. Rev. Immunol.* .
12. Vita, R., S. Mahajan, J. A. Overton, S. K. Dhanda, S. Martini, J. R. Cantrell, D. K. Wheeler, A. Sette, and B. Peters. 2019. The Immune Epitope Database (IEDB): 2018 update. *Nucleic Acids Res.* 47: D339–D343.
13. Antunes, D. A., J. R. Abella, D. Devaurs, M. M. Rigo, and L. E. Kavraki. 2018. Structure-based Methods for Binding Mode and Binding Affinity Prediction for Peptide-MHC Complexes. *Curr. Top. Med. Chem.* 18: 2239–2255.
14. Yanover, C., and P. Bradley. 2011. Large-scale characterization of peptide-MHC binding landscapes with structural simulations. *Proc. Natl. Acad. Sci.* 108: 6981–6986.
15. King, C., E. N. Garza, R. Mazor, J. L. Linehan, I. Pastan, M. Pepper, and D. Baker. 2014. Removing T-cell epitopes with computational protein design. *Proc. Natl. Acad. Sci. U. S. A.* 111: 8577–8582.
16. Liu, T., X. Pan, L. Chao, W. Tan, S. Qu, L. Yang, B. Wang, and H. Mei. 2014. Subangstrom accuracy in pHLA-I modeling by Rosetta FlexPepDock refinement protocol. *J. Chem. Inf. Model.* 54: 2233–2242.
17. Kyeong, H.-H., Y. Choi, and H.-S. Kim. 2018. GradDock: rapid simulation and tailored ranking functions for peptide-MHC Class I docking. *Bioinformatics* 34: 469–476.
18. Rubenstein, A. B., M. A. Pethe, and S. D. Khare. 2017. MFPred: Rapid and accurate prediction of protein-peptide recognition multispecificity using self-consistent mean field theory. *PLoS Comput. Biol.* 13: e1005614.
19. Song, Y., F. DiMaio, R. Y.-R. Wang, D. Kim, C. Miles, T. Brunette, J. Thompson, and D. Baker. 2013. High-Resolution Comparative Modeling with RosettaCM. *Structure* 21: 1735–1742.
20. Frontiers | A Recurrent Mutation in Anaplastic Lymphoma Kinase with Distinct Neoepitope Conformations | Immunology. .
21. Robinson, J., L. A. Guethlein, N. Cereb, S. Y. Yang, P. J. Norman, S. G. E. Marsh, and P. Parham. 2017. Distinguishing functional polymorphism from random variation in the sequences of >10,000 HLA-A, -B and -C alleles. *PLoS Genet.* 13.
22. Berman, H. M., J. Westbrook, Z. Feng, G. Gilliland, T. N. Bhat, H. Weissig, I. N. Shindyalov, and P. E. Bourne. 2000. The Protein Data Bank. *Nucleic Acids Res.* 28: 235–242.
23. Bentzen, A. K., A. M. Marquard, R. Lyngaa, S. K. Saini, S. Ramskov, M. Donia, L. Such, A. J. S. Furness, N. McGranahan, R. Rosenthal, P. T. Straten, Z. Szallasi, I. M. Svane, C. Swanton, S. A. Quezada, S. N. Jakobsen, A. C. Eklund, and S. R. Hadrup. 2016. Large-scale detection of

327 antigen-specific T cells using peptide-MHC-I multimers labeled with DNA barcodes. *Nat.*
328 *Biotechnol.* 34: 1037–1045.
329 24. Saini, S. K., T. Tamhane, R. Anjanappa, A. Saikia, S. Ramskov, M. Donia, I. M. Svane, S. N.
330 Jakobsen, M. Garcia-Alai, M. Zacharias, R. Meijers, S. Springer, and S. R. Hadrup. 2019. Empty
331 peptide-receptive MHC class I molecules for efficient detection of antigen-specific T cells. *Sci.*
332 *Immunol.* 4.
333 25. Overall, S. A., J. S. Toor, S. Hao, M. Yarmarkovich, S. M. O′Rourke, G. I. Morozov, S.
334 Nguyen, A. S. Japp, N. Gonzalez, D. Moschidi, M. R. Betts, J. M. Maris, P. Smibert, and N. G.
335 Sgourakis. High Throughput pMHC-I Tetramer Library Production Using Chaperone-Mediated
336 Peptide Exchange. *Nat. Commun. Press* .
337 26. Ishizuka, J., K. Grebe, E. Shenderov, B. Peters, Q. Chen, Y. Peng, L. Wang, T. Dong, V.
338 Pasquetto, C. Oseroff, J. Sidney, H. Hickman, V. Cerundolo, A. Sette, J. R. Bennink, A.
339 McMichael, and J. W. Yewdell. 2009. Quantitating T Cell Cross-Reactivity for Unrelated
340 Peptide Antigens. *J. Immunol.* 183: 4337–4345.
341 27. Jurtz, V., S. Paul, M. Andreatta, P. Marcatili, B. Peters, and M. Nielsen. 2017. NetMHCpan-
342 4.0: Improved Peptide-MHC Class I Interaction Predictions Integrating Eluted Ligand and
343 Peptide Binding Affinity Data. *J. Immunol. Baltim. Md 1950* 199: 3360–3368.
344 28. Henikoff, S., and J. G. Henikoff. 1992. Amino acid substitution matrices from protein blocks.
345 *Proc. Natl. Acad. Sci. U. S. A.* 89: 10915–10919.
346 29. Chaudhury, S., S. Lyskov, and J. J. Gray. 2010. PyRosetta: a script-based interface for
347 implementing molecular modeling algorithms using Rosetta. *Bioinformatics* 26: 689–691.
348 30. Sievers, F., A. Wilm, D. Dineen, T. J. Gibson, K. Karplus, W. Li, R. Lopez, H. McWilliam,
349 M. Remmert, J. Söding, J. D. Thompson, and D. G. Higgins. 2011. Fast, scalable generation of
350 high-quality protein multiple sequence alignments using Clustal Omega. *Mol. Syst. Biol.* 7: 539.
351 31. Tyka, M. D., D. A. Keedy, I. André, F. Dimaio, Y. Song, D. C. Richardson, J. S. Richardson,
352 and D. Baker. 2011. Alternate states of proteins revealed by detailed energy landscape mapping.
353 *J. Mol. Biol.* 405: 607–618.
354 32. Wu, F., S. Zhao, B. Yu, Y.-M. Chen, W. Wang, Z.-G. Song, Y. Hu, Z.-W. Tao, J.-H. Tian,
355 Y.-Y. Pei, M.-L. Yuan, Y.-L. Zhang, F.-H. Dai, Y. Liu, Q.-M. Wang, J.-J. Zheng, L. Xu, E. C.
356 Holmes, and Y.-Z. Zhang. 2020. A new coronavirus associated with human respiratory disease in
357 China. *Nature* 579: 265–269.
358 33. Kent, W. J., C. W. Sugnet, T. S. Furey, K. M. Roskin, T. H. Pringle, A. M. Zahler, and and
359 D. Haussler. 2002. The Human Genome Browser at UCSC. *Genome Res.* 12: 996–1006.
360 34. Trolle, T., C. P. McMurtrey, J. Sidney, W. Bardet, S. C. Osborn, T. Kaever, A. Sette, W. H.
361 Hildebrand, M. Nielsen, and B. Peters. 2016. The length distribution of class I restricted T cell
362 epitopes is determined by both peptide supply and MHC allele specific binding preference. *J.*
363 *Immunol. Baltim. Md 1950* 196: 1480–1487.
364 35. Mishto, M., and J. Liepe. 2017. Post-Translational Peptide Splicing and T Cell Responses.
365 *Trends Immunol.* 38: 904–915.
366 36. Alford, R. F., A. Leaver-Fay, J. R. Jeliazkov, M. O′Meara, F. P. DiMaio, H. Park, M. V.
367 Shapovalov, P. D. Renfrew, V. K. Mulligan, K. Kappel, J. W. Labonte, M. S. Pacella, R.
368 Bonneau, P. Bradley, R. L. DunbrackJr., R. Das, D. Baker, B. Kuhlman, T. Kortemme, and J. J.
369 Gray. 2017. The Rosetta All-Atom Energy Function for Macromolecular Modeling and Design.
370 *J. Chem. Theory Comput.* 13: 3031–3048.

371 37. Grifoni, A., J. Sidney, Y. Zhang, R. H. Scheuermann, B. Peters, and A. Sette. 2020. A
372 Sequence Homology and Bioinformatic Approach Can Predict Candidate Targets for Immune
373 Responses to SARS-CoV-2. *Cell Host Microbe* .
374 38. Pickett, B. E., E. L. Sadat, Y. Zhang, J. M. Noronha, R. B. Squires, V. Hunt, M. Liu, S.
375 Kumar, S. Zaremba, Z. Gu, L. Zhou, C. N. Larson, J. Dietrich, E. B. Klem, and R. H.
376 Scheuermann. 2012. ViPR: an open bioinformatics database and analysis resource for virology
377 research. *Nucleic Acids Res.* 40: D593–D598.
378 39. Rossjohn, J., S. Gras, J. J. Miles, S. J. Turner, D. I. Godfrey, and J. McCluskey. 2015. T Cell
379 Antigen Receptor Recognition of Antigen-Presenting Molecules. *Annu. Rev. Immunol.* 33: 169–
380 200.
381 40. Rudolph, M. G., R. L. Stanfield, and I. A. Wilson. 2006. How TCRs bind MHCs, peptides,
382 and coreceptors. *Annu. Rev. Immunol.* 24: 419–466.
383 41. Borrman, T., J. Cimons, M. Cosiano, M. Purcaro, B. G. Pierce, B. M. Baker, and Z. Weng.
384 2017. ATLAS: A database linking binding affinities with structures for wild-type and mutant
385 TCR-pMHC complexes. *Proteins Struct. Funct. Bioinforma.* 85: 908–916.
386 42. Riley, T. P., G. L. J. Keller, A. R. Smith, L. M. Davancaze, A. G. Arbuiso, J. R. Devlin, and
387 B. M. Baker. 2019. Structure Based Prediction of Neoantigen Immunogenicity. *Front. Immunol.*
388 10.
389 43. Mallon, D. H., C. Kling, M. Robb, E. Ellinghaus, J. A. Bradley, C. J. Taylor, D. Kabelitz,
390 and V. Kosmoliaptsis. 2018. Predicting Humoral Alloimmunity from Differences in Donor and
391 Recipient HLA Surface Electrostatic Potential. *J. Immunol.* 201: 3780–3792.
392 44. Baker, N. A., D. Sept, S. Joseph, M. J. Holst, and J. A. McCammon. 2001. Electrostatics of
393 nanosystems: application to microtubules and the ribosome. *Proc. Natl. Acad. Sci. U. S. A.* 98:
394 10037–10041.
395 45. Jurrus, E., D. Engel, K. Star, K. Monson, J. Brandi, L. E. Felberg, D. H. Brookes, L. Wilson,
396 J. Chen, K. Liles, M. Chun, P. Li, D. W. Gohara, T. Dolinsky, R. Konecny, D. R. Koes, J. E.
397 Nielsen, T. Head-Gordon, W. Geng, R. Krasny, G.-W. Wei, M. J. Holst, J. A. McCammon, and
398 N. A. Baker. 2018. Improvements to the APBS biomolecular solvation software suite. *Protein*
399 *Sci.* 27: 112–128.
400 46. *The PyMOL Molecular Graphics System*,. Schrödinger, LLC.
401
402

403 **FIGURES**

404

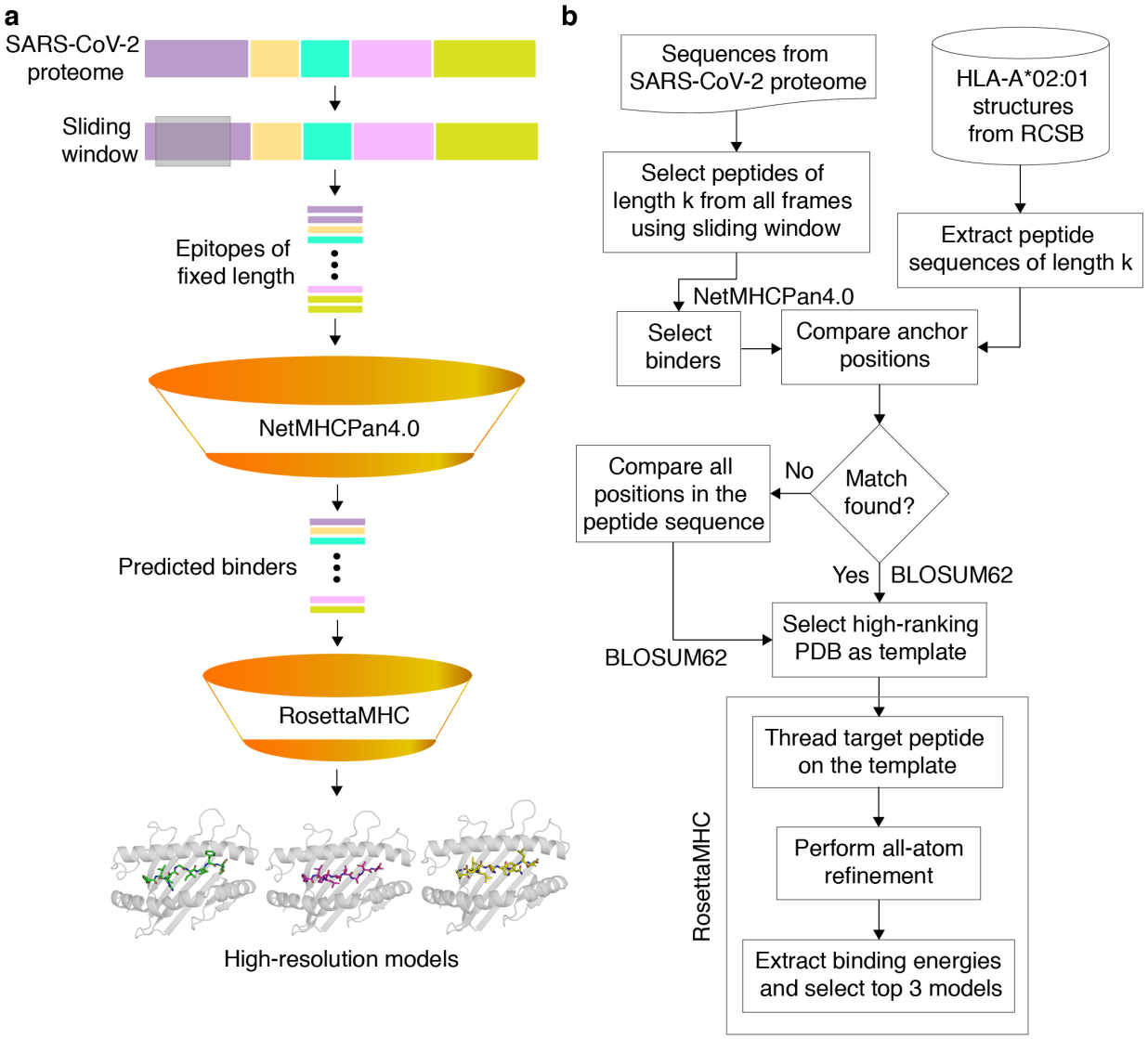

405

406 **FIGURE 1. Structure-guided modeling of T cell epitopes in the SARS-CoV-2 proteome**
407 **(a)** General workflow of our pipeline for structure-guided epitope ranking. **(b)** Protein sequences
408 from the annotated SARS-CoV-2 proteome are used to generate peptide epitopes with a sliding
409 window covering all frames of a fixed length (9,621 9mer and 9,611 10mer possible peptides).
410 Candidate peptides are first filtered by NetMHCpan-4.0 (27) to identify all predicted strong and
411 weak binders (439 9mer and 279 10mer epitopes). For rapid template matching and structure
412 modeling, we use a local database of 241 HLA-A*02:01 X-ray structures with resolution below
413 3.5 Å from the Protein Data Bank (22). Each candidate peptide is scanned against all peptide
414 sequences of the same length in the database, and the top-scoring template is used to guide the
415 RosettaMHC comparative modeling protocol and to compute a binding energy.

416

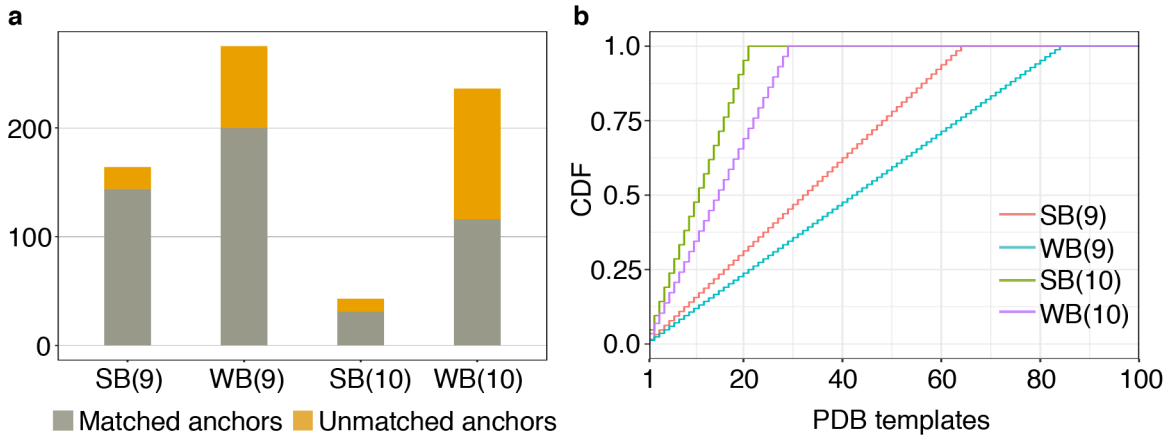

FIGURE 2. Coverage of predicted HLA-A02 epitopes by structural templates in the PDB **(a)** Peptide anchor matching statistics of all predicted SARS-CoV-2 strong (SB) and weak binders (WB) of lengths 9 and 10 to a database of 241 high-resolution HLA-A*02:01 X-ray structures **(b)** Plot showing cumulative distribution (CDF) of strong and weak binder peptides of lengths 9 and 10, as a function of the total number of matching templates from the Protein Data Bank (22).

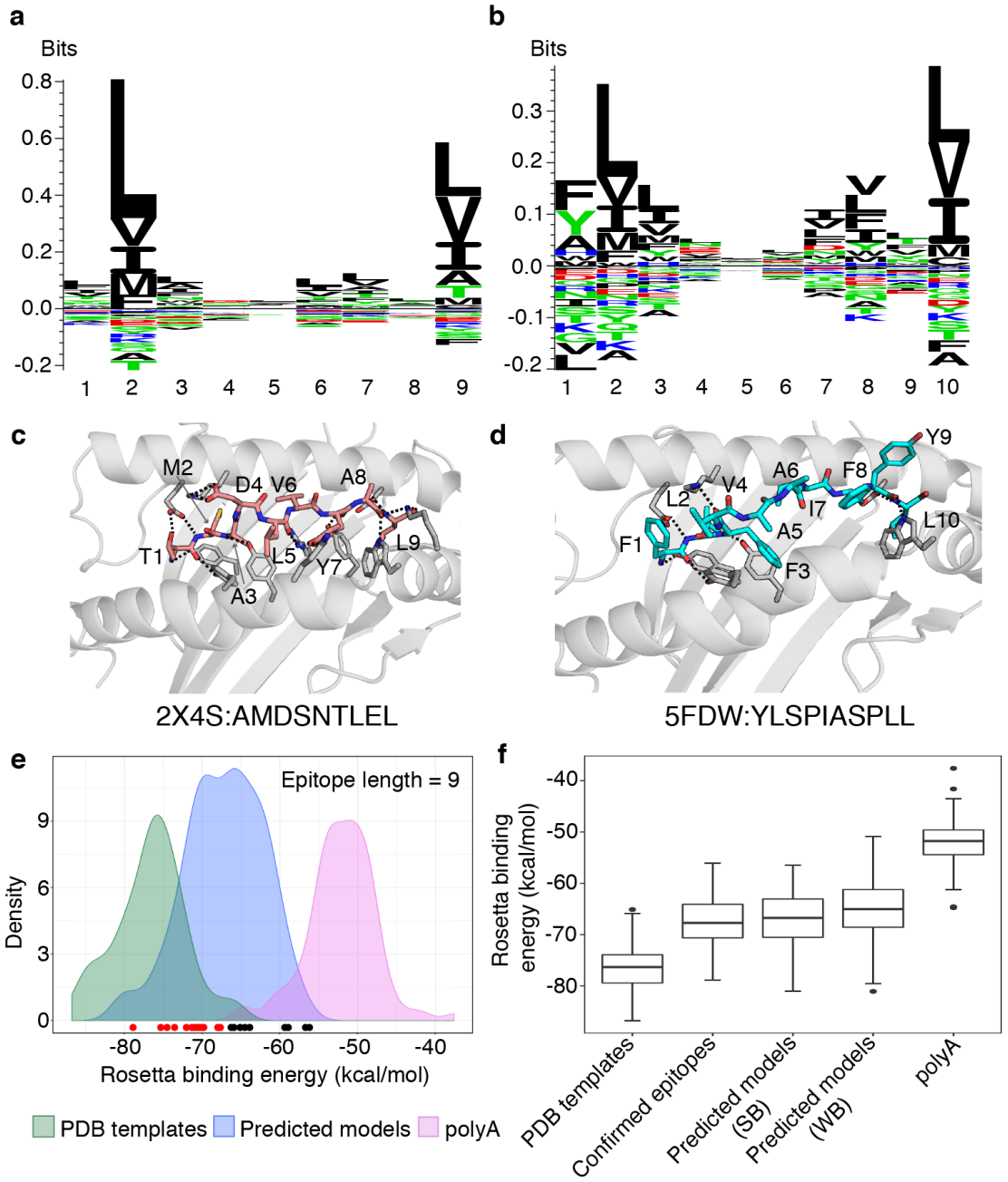

FIGURE 3. Summary of RosettaMHC modeling results for SARS-CoV-2 peptide epitopes Sequence logos from the *n* top ranking epitopes in the SARS-CoV-2 genome, predicted by NetMHCpan-4.0 (27) and further refined using RosettaMHC binding simulations are shown for: **(a)** 9mers (*n*=154) and **(b)** 10mers (*n*=72). The top 9mer and 10mer epitopes in our refined set are shown: **(c)** TMADLVYAL, from RNA polymerase and **(d)** FLFVAAIFYL, from nsp3. Dotted lines indicate polar contacts between peptide and heavy chain residues, with peptide residues labelled. The template PDB IDs and original peptides used for modeling the target peptides are indicated below each model. **(e)** Density plots showing distribution of average Rosetta binding energies (kcal/mol) for all epitopes of length 9. Distributions reflect 93 PDB templates (green),

433 164 strong binder epitopes (according to NetMHCpan-4.0 (27)) (blue), and 93 poly alanine
434 peptides modeled using the same PDB templates and used as a reference set for sub-optimal
435 binders (polyA; pink). The binding energies of models generated for 28 confirmed SARS T cell
436 epitopes from the IEDB and ViPR (37, 38) are indicated by circles at the bottom of the plot. Red
437 circles (19/28) indicate epitopes that lie within the distribution of refined PDB templates and black
438 circles (9/28) indicate epitopes that fall within the distribution of polyA (sub-optimal binders). **(f)**
439 Box plots showing distribution of average binding energies for 93 PDB templates, 93 poly alanine
440 peptides, 28 confirmed epitopes (37, 38) and RosettaMHC models for 164 strong (SB) and 275
441 weak (WB) binder 9mer epitopes predicted from the SARS-CoV-2 proteome using NetMHCpan-
442 4.0 (27).
443

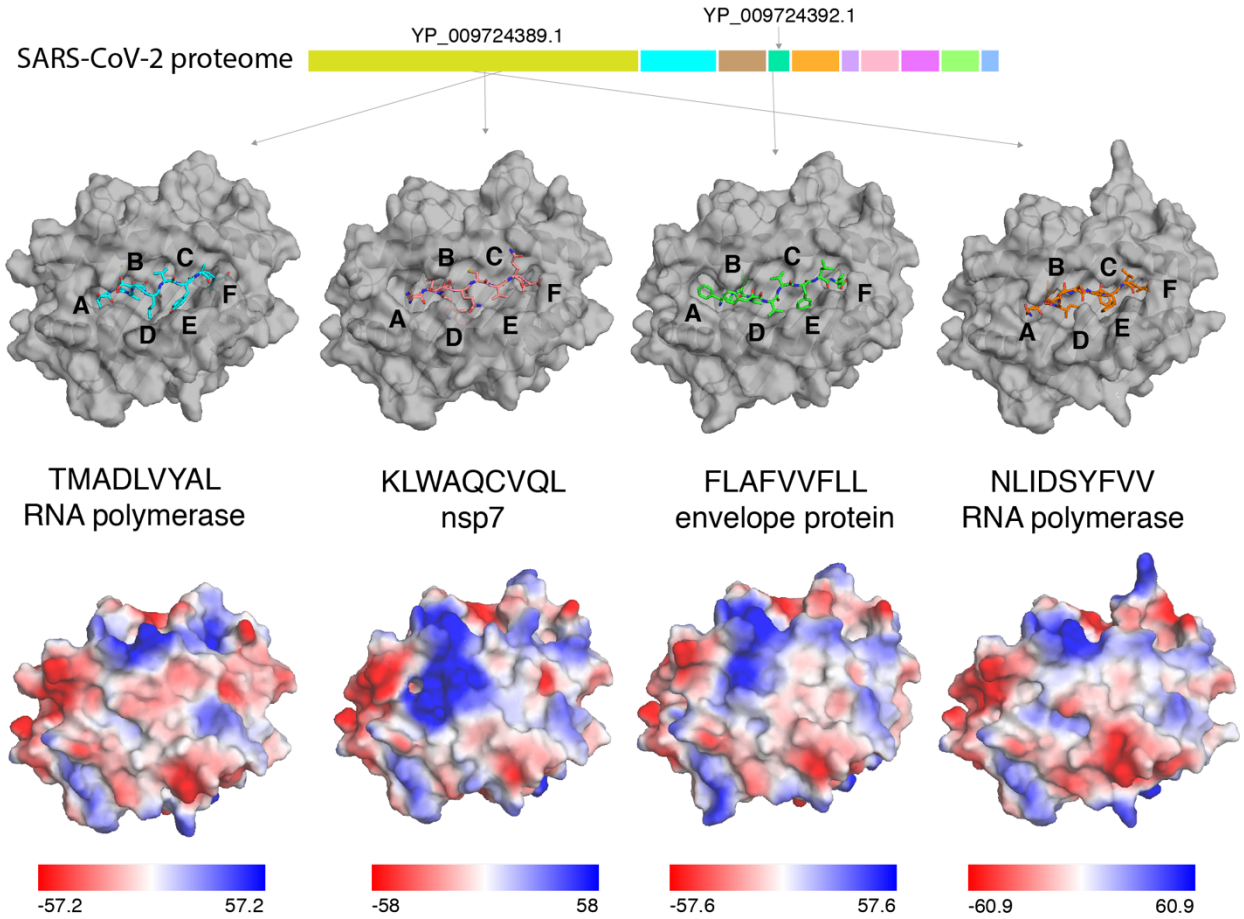

FIGURE 4. Variability in TCR recognition features of HLA-A02 with different high-affinity peptides. Molecular surfaces of SARS-CoV-2/HLA-A*02:01 RosettaMHC models are shown for four top-scoring epitopes (ranked by Rosetta binding energy from left to right) captured in the A, B, C, D, E and F pockets of the MHC-I groove (top panel). The origins of the peptide epitopes in the ~30 kbp SARS-CoV-2 genome are noted. Electrostatic surfaces computed for the same models are shown in the bottom panel. Solvent-accessible surface representation with electrostatic potential in the indicated ranges (down to −60 kcal/(mol·*e*) in red and up to +61 kcal/(mol·*e*) in blue) were calculated using the APBS solver (45) in Pymol (46). All calculations were performed at 150 mM ionic strength, 298.15 Kelvin, pH 7.2, protein dielectric 2.0, and solvent dielectric 78.54. Electrostatic potentials are given in units of kT/e. A 1.4 Å solvent (probe) radius and 10.0 points/$Å^2$ density was used to calculate molecular surfaces.